ACS NANO
Cite This: ACS Nano XXXX, XXX, XXX−XXX
www.acsnano.org

ARTICLE

Quantitative Mapping of the Charge Density in a Monolayer of MoS_2 at Atomic Resolution by Off-Axis Electron Holography

Victor Boureau,*,† Benoit Sklenard,† Robert McLeod,‡ Dmitry Ovchinnikov,¶ Dumitru Dumcenco,¶ Andras Kis,¶ and David Cooper*,†

†Université Grenoble Alpes, CEA, LETI, F-38054 Grenoble, France
‡Université Grenoble Alpes, CEA, INAC, F-38054 Grenoble, France
¶Electrical Engineering Institute, Ecole Polytechnique Federale de Lausanne, CH-1015 Lausanne, Switzerland

Supporting Information

ABSTRACT: The electric potential, electric field, and charge density of a monolayer of MoS_2 have been quantitatively measured at atomic-scale resolution. This has been performed by off-axis electron holography using a double aberration-corrected transmission electron microscope operated at 80 kV and a low electron beam current density. Using this low dose rate and acceleration voltage, the specimen damage is limited during imaging. In order to improve the sensitivity of the measurement, a series of holograms have been acquired. Instabilities of the microscope such as the drifts of the specimen, biprism, and optical aberrations during the acquisition have been corrected by data processing. Phase images of the MoS_2 monolayer have been acquired with a sensitivity of $2\pi/698$ rad associated with a spatial resolution of 2.4 Å. The improvement in the signal-to-noise ratio allows the charge density to be directly calculated from the phase images using Poisson's equation. Density functional theory simulations of the potential and charge density of this MoS_2 monolayer were performed for comparison to the experiment. The experimental measurements and simulations are consistent with each other, and notably, the charge density in a sulfur monovacancy (V_S) site is shown.

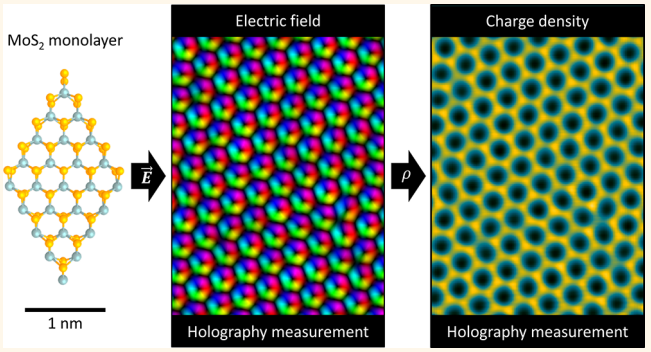

KEYWORDS: *electron holography, high-resolution, MoS_2, charge density, electric potential, electric field, sulfur vacancy*

The emergence of 2D materials[1] for the fabrication of nanoelectronic devices[2−6] requires the influence of the electrical properties of their defects, either at the scale of single atoms such as dopants,[7] impurities,[8] and vacancies[9] or linear such as lines of vacancies[10] and grain boundaries,[11] to be known at an atomic level. This information is essential for a deep understanding and optimization of the macroscopic properties of future devices.[12] The latest generation of transmission electron microscopes (TEM) allows imaging[13,14] or spectroscopic measurements[15,16] of defects to be performed in 2D materials at the atomic level, thus giving insights on the local electrical properties of these defects. Nevertheless the direct observation of the electrical characteristics at an atomic scale remains challenging. For that purpose, recent developments in pixelated scanning transmission electron microscopy (STEM) have been used to measure the electric field and charge density in 2D materials, by scanning a probe on a specimen and locally measuring the changes from the center of mass of the transmitted beam.[17−20] An alternative approach is off-axis electron holography, which is a TEM-based technique that is sensitive to the local electric potential.[21−23] However, it is still a difficult task to both locally and quantitatively measure the electric potential, field, and charge density in these materials with the required sensitivity and spatial resolution.

Typically off-axis electron holography is performed using a weak Lorentz lens, which allows a wide field of view of hundreds of nanometers, but a low spatial resolution of typically 2−6 nm to be obtained. This technique is used widely for the quantitative examination of electric potentials, such as in silicon devices[24] or III−V materials,[25] but also for magnetic field[26] and strain field[27] measurements. However, when using the conventional objective lens, the measurement of electric potentials at atomic resolution can be performed at the

Received: August 24, 2019
Accepted: December 10, 2019
Published: December 10, 2019

DOI: 10.1021/acsnano.9b06716
ACS Nano XXXX, XXX, XXX−XXX

expense of the field of view, which is typically in the range of tens of nanometers. This high-resolution electron holography method was originally conceived as a method to improve the spatial resolution of TEM images by numerically correcting the instrumental aberrations after the hologram reconstruction by using a phase plate.[28] Despite excellent progress with the developments of these methods,[29,30] the experimental challenge and difficulties to interpret atomic-resolution phase images of crystals thicker than a few nanometers because of dynamical scattering[22,31] have meant that this approach has never become widespread. Nevertheless, high-resolution holography is well adapted for the measurement of potentials in 2D materials of a few monolayers, if a sufficient signal-to-noise ratio can be obtained without damaging the sample.[21,22] For holography, the sensitivity is inversely proportional to the spatial resolution;[32] it is still a hard task to reach at the same time an atomic-scale resolution and a very high phase sensitivity.

Here, we show a measurement of the electric potential of a MoS_2 monolayer performed by off-axis electron holography, with atomic-scale spatial resolution combined with high phase sensitivity. This high sensitivity measurement allows the electric field and charge density to be directly mapped at the atomic scale. We show that the quantitative measurements are consistent with density functional theory (DFT) simulations, and this comparison allows for the identification of a sulfur monovacancy (V_S) in the 2D crystal lattice.

RESULTS AND DISCUSSION

Off-axis electron holography experiment uses an electron biprism to interfere a coherent electron wave that has passed through a region of interest with a wave that has passed through a field-free vacuum reference region. This forms an interference pattern known as a hologram. The electron hologram allows the phase and amplitude images to be obtained using a Fourier reconstruction process (see Supporting Information A). In the weak phase object approximation, as is the case for a crystal monolayer, the electron phase ϕ is related to the electromagnetic potential of the specimen by

$$\phi(\mathbf{r}) = \frac{e}{\hbar v}\int_{-\infty}^{+\infty} V(\mathbf{r}, z)\,\mathrm{d}z - \frac{e}{\hbar}\int_{-\infty}^{+\infty} \mathbf{A}_{\parallel}(\mathbf{r}, z)\,\mathrm{d}z \quad (1)$$

where z is the propagation direction of the beam, $\mathbf{r}$ is a position vector perpendicular to it, V is the electric potential, $\mathbf{A}_{\parallel}$ is the contribution of the magnetic vector potential parallel to z, v is the relativistic electron velocity, and e is the elementary charge. The first term describes the electric phase shift, which is proportional to the electric potential projected over the beam propagation. The second term describes the magnetic phase shift, which is proportional to the component of the magnetic vector potential that is parallel to the beam direction and projected over the beam propagation. In the absence of magnetic fields, as is the case for most 2D materials, the electron phase can be directly linked to the electric potential. Next, from the potential, the electric field $\mathbf{E}$ and the charge density ρ can be calculated for a conservative electric field from

$$\mathbf{E}(\mathbf{r}) = -\nabla V(\mathbf{r}) \quad (2)$$

and by applying Gauss's law,

$$\rho(\mathbf{r}) = \varepsilon_0 \nabla\cdot\mathbf{E}(\mathbf{r}) \quad (3)$$

The sensitivity of holography experiments is usually characterized by the phase error (σ_φ) of the measurement. It is given by the phase standard deviation of the measurement in a flat region (*e.g.*, vacuum) or directly at the sample location in the case of recording multiple holograms with the method proposed by McLeod *et al.*[33] The phase sensitivity is improved with an increase of the hologram contrast (μ), an increase of the mean number of electron counts per pixel in the hologram (N_e), or a reduction of the spatial resolution (R), as described by[34,35]

$$\sigma_\varphi \propto \frac{1}{\mu\sqrt{N_e}R} \quad (4)$$

Equaton 4 shows that for high-sensitivity measurements a high electron dose is required. But to limit the beam damage of the specimen, a combination of low electron beam current density and long exposure time is required. Thus, a series of holograms are acquired, leading to the need to correct for the microscope and specimen instabilities over the acquisition time during data processing.[32,33,36] The reconstruction of the high-sensitivity phase image is not straightforward for phase measurements at an atomic scale, as the specimen will drift as well as the electron biprism and the beam wavefront. In addition, at 80 kV the fist-order optical aberrations of the imaging system, such as defocus and 2-fold astigmatism, are unstable in the minute time scale;[37] thus their drift will need to be corrected within the series (see Supporting Information B).

One of the constraints of using off-axis electron holography is that the observed area of the specimen must be close to a region of vacuum that is used to provide the reference wave. This need makes the observation of 2D materials difficult, as the edges of the specimen are often less stable and the layers can be bent, as well as damaged and contaminated. Figure 1(a) shows a conventional high-resolution (HR)-TEM image of the MoS_2 monolayer, close to an edge, acquired before the holography measurement. One can see at the top left of the HR image a hole in the layer caused by beam damage induced by focusing the electron probe at this location, and contrast from residual poly(methyl methacrylate) (PMMA) used for sample preparation (see Methods) is also present in the image. A region having a clean area containing only a monolayer was found. Figure 1(b) shows a single hologram acquired in this region with the analyzed subarea magnified in the inset. The interference fringes with a spacing of 0.077 nm can be clearly observed. A series of 89 holograms, each for 4 s and lasting for a total time period of 7 min and 24 s, were acquired with an electron beam current density of 8.1×10^3 $e^-\cdot Å^{-2}\cdot s^{-1}$ (see Methods). The beam-induced degradation of the sample remains negligible during the acquisition time. Introduction of beam damage is limited by the use of a 80 kV acceleration voltage of the electron beam. The threshold for knock-on damages in MoS_2 is about 90 kV.[38] Moreover the crystal defects are also stable, as supposed by Komsa *et al.*,[39] who show a V_S displacement of 0.0023 atomic jump per second for a TEM experiment with a beam current density of 1.3×10^4 $e^-\cdot Å^{-2}\cdot s^{-1}$, significantly larger than the one we use.

The series of electron holograms were reconstructed with a spatial resolution of 0.24 nm, limited by a numerical aperture during the process (see Supporting Information A). It includes the $\{\bar{1}100\}$ set of planes to give rise to the HR phase maps. The Holoview software, which was written at CEA specifically for this application,[32] was used for the reconstruction. This

DOI: 10.1021/acsnano.9b06716
ACS Nano XXXX, XXX, XXX−XXX

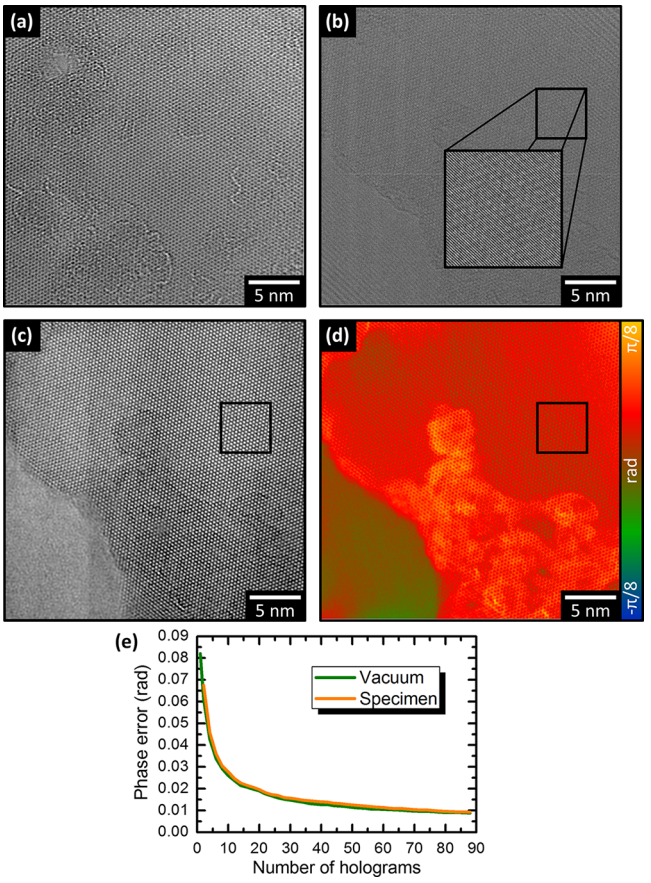

Figure 1. (a) High-resolution TEM image of the MoS_2 monolayer specimen. (b) Single hologram of the MoS_2 specimen, with an inset to visualize the hologram fringes. (c) Amplitude and (d) phase images of the MoS_2 specimen reconstructed from the hologram series. The subarea in (b)−(d) defines the region considered later in the article. (e) Plot of the phase errors measured in the vacuum region and in the specimen subarea, according to the number of holograms used for the reconstruction.

software corrects the mechanical (specimen and biprism) and optical (wavefront and first-order aberrations) drifts that occur during the acquisition time of the series (see Supporting Information B). Then the residual aberrations of the optical system were corrected up to the third order by the use of a phase plate applied to the final complex image (see Supporting Information C). Figure 1(c) shows respectively the reconstructed amplitude and (d) phase images over the whole field of view of the holography experiment, of 33 nm. A vacuum region is observed in the bottom left of these images, as well as the hydrocarbon contamination at the edge and multilayers of MoS_2 and residual PMMA (see Methods) at the bottom. However, a large region of clean 2H-phase MoS_2 monolayer is also present, a few tens of nanometers from the vacuum region. This study will focus on the subarea defined in this region (Figure 1(b−d)).

Figure 1(e) shows the phase errors measured in the analyzed subarea of the specimen and in the vacuum region, according to the number of holograms used for the reconstruction. The phase error decreases from $2\pi/76$ rad for the use of a single hologram to $2\pi/698$ rad for the series reconstructed with 89 holograms, achieving a gain of signal-to-noise ratio close to one order of magnitude. The phase error is inversely proportional to the square root of the number of holograms, as described by eq 4. An advantage of recording a hologram series is the opportunity to assess during data processing whether or not the specimen was subjected to beam degradation. For example, Figure 1(e) shows that the phase error in the specimen stays very close to the one in vacuum over the accumulation of holograms. It is a good figure of merit which indicates that the specimen is not noticeably degraded over the acquisition time of the series.[40] In addition, it gives the ability to reconstruct small subsets of the series along the acquisition time, with lower but sufficient phase sensitivity, to verify further if the sample remains undamaged.

Figure 2(a) shows the experimentally acquired electric potential map of the MoS_2 monolayer, calculated from eq 1. As

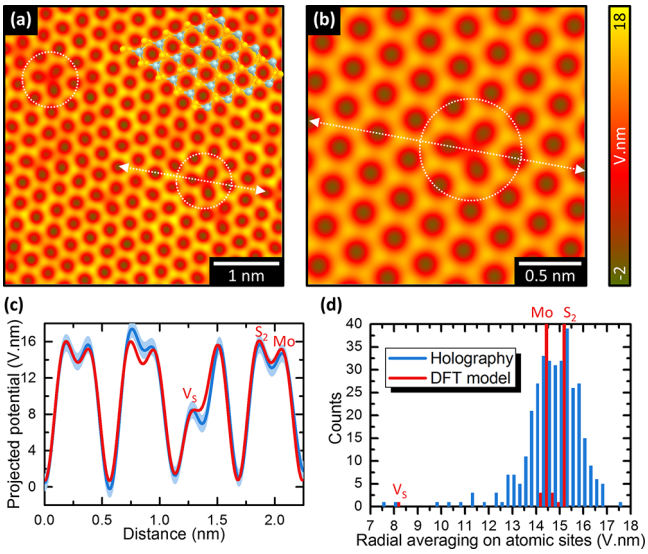

Figure 2. (a) Experimental projected potential measurement of the MoS_2 monolayer calculated from the holography phase image, where the structure of MoS_2 is superimposed to indicate the location of the Mo (gray) and S (yellow) atoms. The presence of two main sites that appear to contain a defect in the crystal are circled. (b) DFT simulation of the projected potential of a MoS_2 monolayer, with a V_S defect encircled. (c) Experimental and simulated profiles of the projected potential extracted across 8 atomic sites including the V_S defect, as indicated by the double arrows in (a) and (b). The experimental error is in light blue. (d) Experimental and simulated histograms of the projected potential taken at the location of each atomic site and averaged over a radius of 0.5 Å.

the thickness of a monolayer remains elusive, we show the projection of the potential over the electron beam path displayed in units of *V·nm*. The structure of MoS_2 is superimposed to indicate the position of the single Mo atoms indicated in gray and the two S atoms in yellow. This experimental map reveals the presence of two main sites that appear to contain a defect in the crystal, indicated within the dashed circles. A splitting of the series into subsets of 10 holograms allowed to verify whether these defects were introduced or moved during the acquisition time of the series and demonstrated that the defect on the left side was introduced by knock-on damage during the beginning of the acquisition, whereas the one on the right side remains stable over the whole acquisition time (see Supporting Information D). Thus, only the stable (right-side) defect is considered here. DFT simulations have been used to simulate the electric

DOI: 10.1021/acsnano.9b06716
ACS Nano XXXX, XXX, XXX−XXX

potential of a 2H-MoS_2 monolayer containing a sulfur monovacancy (see Methods). The simulated projected potential by DFT is shown in Figure 2(b), and the V_S defect is located in the dashed circle. Overall, a good agreement is observed between the measurement (Figure 2(a)) and the simulation (Figure 2(b)). The average value of the potential, corresponding to the mean inner potential of the MoS_2 monolayer, is found to be 10.4 V·nm experimentally and 10.6 V·nm by simulation.

The profiles taken from across the regions indicated by the dashed lines in Figure 2(a) and (b) are shown in Figure 2(c). This quantitative comparison between the experimental and simulated projected potentials demonstrates a good agreement. The experimental error bar in light blue corresponds to the phase error of the measurement. The DFT shows that the differences in the projected electric potential in the Mo and S_2 sites is small, respectively 15.2 and 16.0 V·nm, whereas the potential located at the V_S defect is 8.5 V·nm. The good quantitative agreement between the holography measurement and the modeling allows the crystal defect to be clearly identified as a sulfur monovacancy from the experimental potential map. Figure 2(d) plots the histogram of the projected potential taken at the location of each atomic site and averaged over a radius of 0.5 Å for both the holography measurement and DFT simulation. Based on the modeling, Mo and S_2 sites show in the histogram a radial averaging of 14.5 and 15.25 V nm, respectively. A statistical dispersion around these values is observed experimentally, resulting from the accuracy of the measurement. The few experimental values far below these reference values, typically below 13 V·nm, result from atomic defects that possibly evolve (creation, annihilation, displacement) under the electron beam during the acquisition time of the hologram series. In the histogram, the averaged projected potential of the V_S shows a value of 8.25 V·nm from the DFT model. It is again in good agreement with the experimental one, visible at 8.0 V·nm.

Figure 3(a) shows the holography measurement of the electric field projected over the electron beam path, thus displayed in units of *V*. Figure 3(b) is the projected electric field obtained from the DFT simulation. These maps are proportional to the gradient of the projected electric potential, which is calculated using eq 2. It is solely sensitive to the electric field in the observation plane $\mathbf{E}_\perp$, *i.e.*, perpendicular to the electron beam direction. The MoS_2 structure is superimposed onto the experimental image to indicate the location of the atom sites. The location of the V_S defect is circled on both the experimental and simulated maps. These maps show the quantitative distribution of the electric field in the MoS_2 monolayer at the atomic scale, though limited by the spatial resolution of the measurement of 2.4 Å. Overall, a good quantitative agreement is observed on the projected electric field, between the measurement and the DFT model. The electric field modulation around the V_S defect is clear from the simulation in Figure 3(b), showing a triangular dark shape that compares well to the measurement in Figure 3(a).

Figure 4(a) shows the holography measurement of the charge density, projected over the electron beam path. Thus,

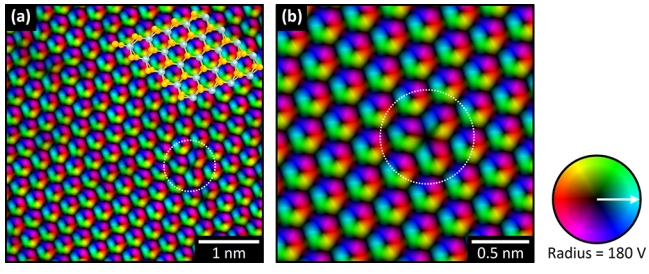

Figure 3. (a) Experimental measurement of the projected electric field, $\mathbf{E}_\perp$, of the MoS_2 monolayer calculated from the holography phase image. The structure of MoS_2 is superimposed to indicate the location of the Mo (gray) and S (yellow) atoms. The presence of the identified V_S site is indicated. (b) Simulation of the projected electric field, $\mathbf{E}_\perp$, of a MoS_2 monolayer with a V_S defect indicated, calculated from the DFT simulation. These vector fields are encoded in the color wheel, where their orientation is given by the color and their modulus is given by the saturation, increasing along the radius from 0 to 180 V.

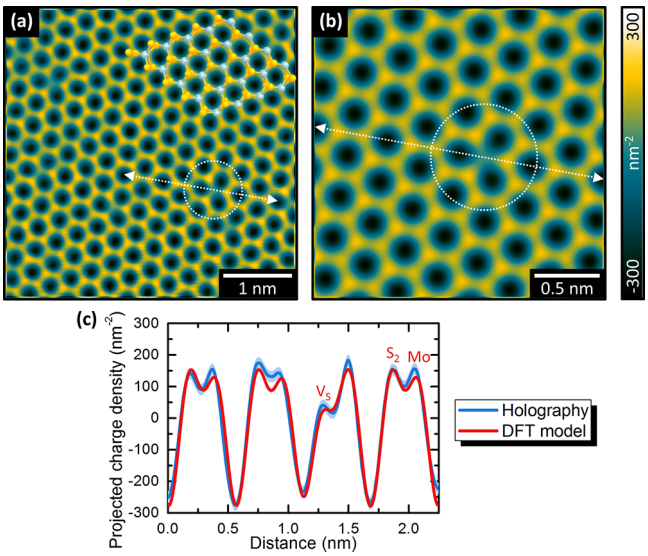

Figure 4. (a) Experimental projected charge density of the MoS_2 monolayer calculated from the holography phase image, where the structure of MoS_2 is superimposed to indicate the location of the Mo (gray) and S (yellow) atoms. The presence of the identified V_S site is indicated. (b) DFT simulation of the projected charge density of a MoS_2 monolayer, with a V_S defect indicated. (c) Experimental and simulated profiles of the projected charge density extracted across 8 atomic sites including the V_S defect, as indicated by the double arrows in (a) and (b). The experimental error is in light blue.

the charge density is quantified as a number of charges per unit area, in units of nm^{-2}. The positive values come from the proton charge contribution of atomic nuclei, while the negative values come from the electron charge contribution. This map is proportional to the divergence of the electric field; see eq 3. Therefore, the Laplacian of the projected potential is performed (applying eqs 2 and 3 to give Poisson's equation), in order to make possible a direct access to the experimental charge density. Here, the very low experimental phase error permits this double derivative to be applied while maintaining a sufficient signal-to-noise ratio for the quantitative analysis of the charge density map. Figure 4(b) is the projected charge density obtained directly from DFT simulation (see Methods). Again, the MoS_2 structure is superimposed on the experimental image to indicate the location of the atomic sites, and the location of the V_S defect is indicated on both experimental and simulated maps. A good agreement between the experimental

DOI: 10.1021/acsnano.9b06716
ACS Nano XXXX, XXX, XXX−XXX

and simulated projection of the charge density is observed in these images. Due to the charge neutrality of the system, the mean value of the projected charge density maps is 0 nm^{-2}. Profiles have been extracted from the indicated lines and are shown in Figure 4(c). The projected charge density modeled by DFT for the Mo and S_2 atomic sites' location is similar, being 130 and 150 nm^{-2}, respectively. The value for the V_S defect position is 30 nm^{-2}. The positive values mean that the proton charges from the atomic nuclei account for the main contribution of charge density around the atomic positions. In the center of the hexagonal structure, the charge density drops down to −280 nm^{-2}, hence dominated by the negative charges from the electrons. The holography measurement shows a good quantitative agreement with the simulation, including at the V_S location, as depicted in Figure 4(c). Thus, the crystal defect measured by holography can also be well identified as a sulfur monovacancy from the charge density map, with respect to the simulation.

These measurements are consistent with recent reports of the fields measured in MoS_2 specimens using center of mass pixelated STEM techniques.[18,20] Compared to holography, pixelated STEM techniques have a better spatial resolution but often need to average the signal of several crystal unit cells over the field of view in order to obtain a good signal-to-noise ratio. However, with holography the signal is averaged over time, allowing to track the influence of the electron beam on the structure. We therefore demonstrate that the quantitative measurement of the charge density by off-axis electron holography is a powerful tool that can be used to validate DFT simulations of 2D materials with the prospect of extending the study to different types of materials and defects such as grain boundaries and dopant atoms.

CONCLUSIONS

We have shown that by using high-resolution off-axis electron holography it is possible to quantitatively measure the local charge densities with atomic resolution in monolayers of 2D materials. In order to achieve the required signal-to-noise ratio, a methodology to acquire a large series of holograms has been developed while using a low electron beam current density to limit the damage to the specimen. The key to these measurements is to be able to correct the drift of the specimen, biprism, and low-order aberrations between each phase image from the hologram series. The high signal-to-noise ratio in the projected potential maps allows Poisson's equation to be used to extract the charge density. These results are in agreement with DFT simulations, suggesting that our measurement is accurate. Although our methodology works using a state-of-the-art double aberration-corrected transmission electron microscope, there are many improvements that could be made in order to make this an easier and thus more routine experiment. First, this work has been performed using a single biprism system, and as such, it is necessary to take measurements near a region of vacuum. In this case the specimen is often less mechanically stable and also dirty, which makes it difficult to find a suitable region of interest. By using a multiple biprism system it is possible to acquire the reference far from the region of interest as well as increase the spatial resolution.[41,42] Indeed the possibility to take measurements far from a region of vacuum would allow interesting defect structures and grain boundaries to be more easily studied. In addition, this approach could be combined with the use of very low energy electron beams in the range 20−60 kV, which could prevent the effects of knock-on damage, increase the stability of crystal defects under the beam, and allow specimens to be examined for longer time periods.[43] Of course the use of hybrid pixel detectors[44] would improve sensitivity in the reconstructed phase images. This approach also requires further developments in the number of pixels, such that the interference fringes can be correctly sampled while maintaining a reasonable field of view of the measurement. Although the methods presented here will surely be improved, we show that it is possible today to locally measure the charge density with atomic resolution, and as such, the electronic structure around specific atoms or defects can be measured. With this methodology, it will be possible to obtain valuable information about the electronic structure of defects, such as dopants and grain boundaries, in a range of different 2D materials to be able to accelerate the design and development of electronic devices based on these materials.

METHODS

Specimen Preparation. Epitaxial monolayer MoS_2 samples were grown by CVD onto c-plane sapphire.[45] To produce a free-standing monolayer for TEM analysis, a PMMA film was spin coated at 1500 rpm onto the wafer, which was then immersed in KOH (30% weight) at 70 °C for 20 min to detach the PMMA film with the MoS_2 from the substrate. The floating PMMA membrane was transferred to deionized water to remove the KOH residue. The MoS_2 monolayers were then transferred on top of holey Si_3N_4 TEM grids. The PMMA was removed by annealing in Ar/H_2 atmosphere at 400 °C for 8 h. Before being put into the electron microscope the MoS_2 specimen was annealed at a temperature of 120 °C overnight in vacuum to release organic contamination.

Transmission Electron Microscopy. TEM experiments were performed using a double aberration-corrected FEI Titan Ultimate operated at 80 kV. The probe corrector was used to provide a flat wavefront of the electron beam, and the image corrector to provide atomic-scale resolution in TEM mode. To provide the optimum compromise between fringe spacing, contrast, and field of view, the diffraction lens was excited to 65% and the specimen focus adjusted by changing the height of the specimen. A low dose rate of 0.13 pA nm^{-2} was chosen in order to limit the specimen damage. A 4k × 4k $pixel^2$ Gatan OneView camera was used to record the electron holograms. The specimen orientation was finely tuned to be directly on the [0001] zone axis prior to acquisition, by looking at the live fast Fourier transform of the hologram and considering the diffraction spots from the side-bands, which are very sensitive to the crystal orientation. A series of 89 electron holograms with a field of view of 33 nm and a fringe spacing of 0.077 nm was acquired, each for 4 s with a dead time of 1 s in-between each. Each fringe was sampled using 9 pixels to provide a reasonable value of contrast in each hologram, of 17%, with a mean intensity of 90 electrons detected per pixel for each individual acquisition. A series of 10 reference holograms was acquired in vacuum with the same parameters, immediately after the acquisition of the series of holograms of the specimen. The data were processed using the Holoview software[32] developed at CEA LETI, which aligns the specimen drift, biprism drift, wavefront drift, and low-order aberration drift to provide reconstructed phase images with high enough sensitivity to apply Poisson's law to calculate the charge density with atomic resolution (see Supporting Information for more details).

Simulation. *Ab initio* calculations based on DFT were carried out using the VASP code.[46,47] We used DFT within the generalized-gradient approximation (GGA) of Perdew, Burke, and Ernzerhof (PBE).[48] The core−valence interaction was described with projector augmented wave (PAW) data sets including $4s^24p^65s^14d^5$ and $3s^23p^4$ for Mo and S, respectively. Electron wave functions were expanded in a plane wave basis set with a kinetic energy cutoff of 400 eV. We first relaxed the structure of monolayer (ML) MoS_2 using a 14 × 14 × 1 Γ-centered Monkhorst−Pack mesh to sample the Brillouin zone and a

DOI: 10.1021/acsnano.9b06716
ACS Nano XXXX, XXX, XXX−XXX

30 Å vacuum in the *c* direction (*i.e.*, perpendicular to the ML) to prevent spurious interactions between periodic images. V_S point defect calculations were performed using a 240-atom orthogonal supercell with 30 Å vacuum, and the Brillouin zone was sampled at the Γ point. The V_S configuration was relaxed until the residual force for each atom was less than 0.01 eV·Å^{-1}. The charge density and potential were then computed on a finer grid with a resolution of 0.025 Å to reconstruct the all-electron maps (*i.e.*, including core electrons). The contribution of protons was added assuming point charges at the positions of the nuclei.

Finally, the same low-pass filter (numerical aperture) as for the reconstruction of holograms (see Supporting Information A) has been used to convolute the maps modeled by DFT, in order to compare the simulation to the holography measurements with the exact same spatial resolution. Indeed the limited spatial resolution of the measurement induces a spreading of the experimental maps and thus a damping of the magnitude of their values.

ASSOCIATED CONTENT

Supporting Information

The Supporting Information is available free of charge at https://pubs.acs.org/doi/10.1021/acsnano.9b06716.

> Fourier reconstruction process of holograms; sample, biprism, wavefront, and aberration drift corrections; residual aberration correction with a phase plate; stability of the crystal defects by the use of subsets of hologram series (PDF)

AUTHOR INFORMATION

Corresponding Authors

*E-mail: victor.boureau@epfl.ch.
*E-mail: david.cooper@cea.fr.

ORCID

Victor Boureau: 0000-0001-6251-5892
Andras Kis: 0000-0002-3426-7702
David Cooper: 0000-0003-3479-4374

Notes

The authors declare no competing financial interest.

ACKNOWLEDGMENTS

D.C. thanks the European Research Council for the Starting Grant Stg: 306535 Holoview for funding. The TEM experiments were performed on the Nanocharacterisation platform at Minatec, Grenoble. R.M. thanks the Nanosciences Foundation for funding.

REFERENCES

(1) Geim, A. K.; Grigorieva, I. V. Van der Waals Heterostructures. *Nature* **2013**, *499*, 419−425.
(2) Wang, Q. H.; Kalantar-Zadeh, K.; Kis, A.; Coleman, J. N.; Strano, M. S. Electronics and Optoelectronics of Two-Dimensional Transition Metal Dichalcogenides. *Nat. Nanotechnol.* **2012**, *7*, 699−712.
(3) Radisavljevic, B.; Radenovic, A.; Brivio, J.; Giacometti, V.; Kis, A. Single-Layer MoS_2 Transistors. *Nat. Nanotechnol.* **2011**, *6*, 147−150.
(4) Bertolazzi, S.; Krasnozhon, D.; Kis, A. Nonvolatile Memory Cells Based on MoS_2/Graphene Heterostructures. *ACS Nano* **2013**, *7*, 3246−3252.
(5) Lopez-Sanchez, O.; Lembke, D.; Kayci, M.; Radenovic, A.; Kis, A. Ultrasensitive Photodetectors Based on Monolayer MoS_2. *Nat. Nanotechnol.* **2013**, *8*, 497−501.
(6) Ross, J. S.; Klement, P.; Jones, A. M.; Ghimire, N. J.; Yan, J.; Mandrus, D. G.; Taniguchi, T.; Watanabe, K.; Kitamura, K.; Yao, W.; Cobden, D. H.; Xu, X. Electrically Tunable Excitonic Light-Emitting Diodes Based on Monolayer WSe_2 *P*−*N* Junctions. *Nat. Nanotechnol.* **2014**, *9*, 268−272.
(7) Terrones, H.; Lv, R.; Terrones, M.; Dresselhaus, M. S. The Role of Defects and Doping in 2D Graphene Sheets and 1D Nanoribbons. *Rep. Prog. Phys.* **2012**, *75*, 062501.
(8) Ni, Z. H.; Yu, T.; Luo, Z. Q.; Wang, Y. Y.; Liu, L.; Wong, C. P.; Miao, J.; Huang, W.; Shen, Z. X. Probing Charged Impurities in Suspended Graphene Using Raman Spectroscopy. *ACS Nano* **2009**, *3*, 569−574.
(9) Qiu, H.; Xu, T.; Wang, Z.; Ren, W.; Nan, H.; Ni, Z.; Chen, Q.; Yuan, S.; Miao, F.; Song, F.; Long, G.; Shi, Y.; Sun, L.; Wang, J.; Wang, X. Hopping Transport Through Defect-Induced Localized States in Molybdenum Disulphide. *Nat. Commun.* **2013**, *4*, 2642.
(10) Wang, S.; Lee, G.-D.; Lee, S.; Yoon, E.; Warner, J. H. Detailed Atomic Reconstruction of Extended Line Defects in Monolayer MoS_2. *ACS Nano* **2016**, *10*, 5419−5430.
(11) van der Zande, A. M.; Huang, P. Y.; Chenet, D. A.; Berkelbach, T. C.; You, Y.; Lee, G.-H.; Heinz, T. F.; Reichman, D. R.; Muller, D. A.; Hone, J. C. Grains and Grain Boundaries in Highly Crystalline Monolayer Molybdenum Disulphide. *Nat. Mater.* **2013**, *12*, 554−561.
(12) Lin, Z.; McCreary, A.; Briggs, N.; Subramanian, S.; Zhang, K.; Sun, Y.; Li, X.; Borys, N. J.; Yuan, H.; Fullerton-Shirey, S. K.; Chernikov, A.; Zhao, H.; McDonnell, S.; Lindenberg, A. M.; Xiao, K.; LeRoy, B. J.; Drndić, M.; Hwang, J. C. M.; Park, J.; Chhowalla, M.; et al. 2D Materials Advances: From Large Scale Synthesis and Controlled Heterostructures to Improved Characterization Techniques, Defects and Applications. *2D Mater.* **2016**, *3*, 042001.
(13) Meyer, J. C.; Kurasch, S.; Park, H. J.; Skakalova, V.; Künzel, D.; Groß, A.; Chuvilin, A.; Algara-Siller, G.; Roth, S.; Iwasaki, T.; Starke, U.; Smet, J. H.; Kaiser, U. Experimental Analysis of Charge Redistribution Due to Chemical Bonding by High-Resolution Transmission Electron Microscopy. *Nat. Mater.* **2011**, *10*, 209−215.
(14) Dumcenco, D. O.; Kobayashi, H.; Liu, Z.; Huang, Y.-S.; Suenaga, K. Visualization and Quantification of Transition Metal Atomic Mixing in $Mo_{1-x}W_xS_2$ Single Layers. *Nat. Commun.* **2013**, *4*, 1351.
(15) Zhou, W.; Kapetanakis, M. D.; Prange, M. P.; Pantelides, S. T.; Pennycook, S. J.; Idrobo, J.-C. Direct Determination of the Chemical Bonding of Individual Impurities in Graphene. *Phys. Rev. Lett.* **2012**, *109*, 206803.
(16) Ramasse, Q. M.; Seabourne, C. R.; Kepaptsoglou, D.-M.; Zan, R.; Bangert, U.; Scott, A. J. Probing the Bonding and Electronic Structure of Single Atom Dopants in Graphene with Electron Energy Loss Spectroscopy. *Nano Lett.* **2013**, *13*, 4989−4995.
(17) Müller, K.; Krause, F. F.; Béché, A.; Schowalter, M.; Galioit, V.; Löffler, S.; Verbeeck, J.; Zweck, J.; Schattschneider, P.; Rosenauer, A. Atomic Electric Fields Revealed by a Quantum Mechanical Approach to Electron Picodiffraction. *Nat. Commun.* **2014**, *5*, 5653.
(18) Müller-Caspary, K.; Duchamp, M.; Rösner, M.; Migunov, V.; Winkler, F.; Yang, H.; Huth, M.; Ritz, R.; Simson, M.; Ihle, S.; Soltau, H.; Wehling, T.; Dunin-Borkowski, R. E.; Van Aert, S.; Rosenauer, A. Atomic-Scale Quantification of Charge Densities in Two-Dimensional Materials. *Phys. Rev. B: Condens. Matter Mater. Phys.* **2018**, *98*, 121408.
(19) Ishikawa, R.; Findlay, S. D.; Seki, T.; Sánchez-Santolino, G.; Kohno, Y.; Ikuhara, Y.; Shibata, N. Direct Electric Field Imaging of Graphene Defects. *Nat. Commun.* **2018**, *9*, 3878.
(20) Fang, S.; Wen, Y.; Allen, C. S.; Ophus, C.; Han, G. G.; Kirkland, A. I.; Kaxiras, E.; Warner, J. H. Atomic Electrostatic Maps of 1D Channels in 2D Semiconductors Using 4D Scanning Transmission Electron Microscopy. *Nat. Commun.* **2019**, *10*, 1127.
(21) Cooper, D.; Pan, C.-T.; Haigh, S. Atomic Resolution Electrostatic Potential Mapping of Graphene Sheets by Off-Axis Electron Holography. *J. Appl. Phys.* **2014**, *115*, 233709.
(22) Winkler, F.; Tavabi, A. H.; Barthel, J.; Duchamp, M.; Yucelen, E.; Borghardt, S.; Kardynal, B. E.; Dunin-Borkowski, R. E. Quantitative Measurement of Mean Inner Potential and Specimen Thickness from High-Resolution Off-Axis Electron Holograms of Ultra-Thin Layered WSe_2. *Ultramicroscopy* **2017**, *178*, 38−47.

DOI: 10.1021/acsnano.9b06716
ACS Nano XXXX, XXX, XXX−XXX

(23) Borghardt, S.; Winkler, F.; Zanolli, Z.; Verstraete, M.; Barthel, J.; Tavabi, A.; Dunin-Borkowski, R.; Kardynal, B. Quantitative Agreement Between Electron-Optical Phase Images of WSe_2 and Simulations Based on Electrostatic Potentials That Include Bonding Effects. *Phys. Rev. Lett.* **2017**, *118*, 086101.
(24) Rau, W. D.; Schwander, P.; Baumann, F. H.; Höppner, W.; Ourmazd, A. Two-Dimensional Mapping of the Electrostatic Potential in Transistors by Electron Holography. *Phys. Rev. Lett.* **1999**, *82*, 2614−2617.
(25) Ponce, F. A. Electrostatic Energy Profiles at Nanometer-Scale in Group III Nitride Semiconductors Using Electron Holography. *Ann. Phys. (Berlin, Ger.)* **2011**, *523*, 75−86.
(26) Tonomura, A.; Osakabe, N.; Matsuda, T.; Kawasaki, T.; Endo, J.; Yano, S.; Yamada, H. Evidence for Aharonov-Bohm Effect with Magnetic Field Completely Shielded from Electron Wave. *Phys. Rev. Lett.* **1986**, *56*, 792−795.
(27) Hÿtch, M.; Houdellier, F.; Hüe, F.; Snoeck, E. Nanoscale Holographic Interferometry for Strain Measurements in Electronic Devices. *Nature* **2008**, *453*, 1086−1089.
(28) Lichte, H. Electron Holography Approaching Atomic Resolution. *Ultramicroscopy* **1986**, *20*, 293−304.
(29) Linck, M.; Freitag, B.; Kujawa, S.; Lehmann, M.; Niermann, T. State of the Art in Atomic Resolution Off-Axis Electron Holography. *Ultramicroscopy* **2012**, *116*, 13−23.
(30) Niermann, T.; Lehmann, M. Averaging Scheme for Atomic Resolution Off-Axis Electron Holograms. *Micron* **2014**, *63*, 28−34.
(31) Lichte, H.; Formanek, P.; Lenk, A.; Linck, M.; Matzeck, C.; Lehmann, M.; Simon, P. Electron Holography: Applications to Materials Questions. *Annu. Rev. Mater. Res.* **2007**, *37*, 539−588.
(32) Boureau, V.; McLeod, R.; Mayall, B.; Cooper, D. Off-Axis Electron Holography Combining Hologram Summation with Double-Exposure Phase-Shifting: Theory and Application. *Ultramicroscopy* **2018**, *193*, 52−63.
(33) McLeod, R. A.; Bergen, M.; Malac, M. Phase Measurement Error in Summation of Electron Holography Series. *Ultramicroscopy* **2014**, *141*, 38−50.
(34) Harscher, A.; Lichte, H. Experimental Study of Amplitude and Phase Detection Limits in Electron Holography. *Ultramicroscopy* **1996**, *64*, 57−66.
(35) Voelkl, E. Noise in Off-Axis Type Holograms Including Reconstruction and CCD Camera Parameters. *Ultramicroscopy* **2010**, *110*, 199−210.
(36) Voelkl, E.; Tang, D. Approaching Routine $2\pi/1000$ Phase Resolution for Off-Axis Type Holography. *Ultramicroscopy* **2010**, *110*, 447−459.
(37) Barthel, J.; Thust, A. On the Optical Stability of High-Resolution Transmission Electron Microscopes. *Ultramicroscopy* **2013**, *134*, 6−17.
(38) Komsa, H.-P.; Kotakoski, J.; Kurasch, S.; Lehtinen, O.; Kaiser, U.; Krasheninnikov, A. V. Two-Dimensional Transition Metal Dichalcogenides Under Electron Irradiation: Defect Production and Doping. *Phys. Rev. Lett.* **2012**, *109*, 035503.
(39) Komsa, H.-P.; Kurasch, S.; Lehtinen, O.; Kaiser, U.; Krasheninnikov, A. V. From Point to Extended Defects in Two-Dimensional MoS_2: Evolution of Atomic Structure Under Electron Irradiation. *Phys. Rev. B: Condens. Matter Mater. Phys.* **2013**, *88*, 035301.
(40) Röder, F.; Lubk, A.; Wolf, D.; Niermann, T. Noise Estimation for Off-Axis Electron Holography. *Ultramicroscopy* **2014**, *144*, 32−42.
(41) Harada, K.; Matsuda, T.; Tonomura, A.; Akashi, T.; Togawa, Y. Triple-Biprism Electron Interferometry. *J. Appl. Phys.* **2006**, *99*, 113502.
(42) Tanigaki, T.; Aizawa, S.; Park, H. S.; Matsuda, T.; Harada, K.; Shindo, D. Advanced Split-Illumination Electron Holography Without Fresnel Fringes. *Ultramicroscopy* **2014**, *137*, 7−11.
(43) Kaiser, U.; Biskupek, J.; Meyer, J. C.; Leschner, J.; Lechner, L.; Rose, H.; Stöger-Pollach, M.; Khlobystov, A. N.; Hartel, P.; Müller, H.; Haider, M.; Eyhusen, S.; Benner, G. Transmission Electron Microscopy at 20kV for Imaging and Spectroscopy. *Ultramicroscopy* **2011**, *111*, 1239−1246.
(44) Tate, M. W.; Purohit, P.; Chamberlain, D.; Nguyen, K. X.; Hovden, R.; Chang, C. S.; Deb, P.; Turgut, E.; Heron, J. T.; Schlom, D. G.; Ralph, D. C.; Fuchs, G. D.; Shanks, K. S.; Philipp, H. T.; Muller, D. A.; Gruner, S. M. High Dynamic Range Pixel Array Detector for Scanning Transmission Electron Microscopy. *Microsc. Microanal.* **2016**, *22*, 237−249.
(45) Dumcenco, D.; Ovchinnikov, D.; Marinov, K.; Lazić, P.; Gibertini, M.; Marzari, N.; Sanchez, O. L.; Kung, Y.-C.; Krasnozhon, D.; Chen, M.-W.; Bertolazzi, S.; Gillet, P.; Fontcuberta i Morral, A.; Radenovic, A.; Kis, A. Large-Area Epitaxial Monolayer MoS_2. *ACS Nano* **2015**, *9*, 4611−4620.
(46) Kresse, G.; Furthmüller, J. Efficient Iterative Schemes for *Ab Initio* Total-Energy Calculations Using a Plane-Wave Basis Set. *Phys. Rev. B: Condens. Matter Mater. Phys.* **1996**, *54*, 11169−11186.
(47) Kresse, G.; Joubert, D. From Ultrasoft Pseudopotentials to the Projector Augmented-Wave Method. *Phys. Rev. B: Condens. Matter Mater. Phys.* **1999**, *59*, 1758−1775.
(48) Perdew, J. P.; Burke, K.; Ernzerhof, M. Generalized Gradient Approximation Made Simple. *Phys. Rev. Lett.* **1996**, *77*, 3865−3868.

DOI: 10.1021/acsnano.9b06716
ACS Nano XXXX, XXX, XXX−XXX